Integrated Optical Amplifier-Photodetector on a Wearable Nanocellulose Substrate

Alberto Suárez[1], Ehsan Hassanabadi[2], Alberto Maulu[1], Niccolò Carlino[3], Cecilia Ada Maestri[3], Masoud Latifi[4], Paolo Bettotti[3], Iván Mora-Seró[2] and Juan P. Martínez-Pastor[1]

[1]UMDO, Instituto de Ciencia de los Materiales, Universidad de Valencia, 46071 Valencia, Spain

2Institute of Advanced Materials (INAM), Universitat Jaume I, 12006 Castelló, Spain

3NanoscienceLaboratory, Department of Physics, University of Trento, ViaSommarive 14, 38123, Povo (TN), Italy
4

Flexible optoelectronics has emerged as an outstanding platform to pave the road toward vanguard technology advancements. As compared to conventional rigid substrates, a flexible technology enables mechanical deformation while maintaining stable performance. The advantages include not only the development to novel applications, but also the implementation of a wearable technology directly in contact with a curved surface. Here we show the monolithic integration of a perovskite-based optical waveguide amplifier, together with a photodetector on a nanocellulose substrate to demonstrate the feasibility of a stretchable signal manipulation and receptor system fabricated on a biodegradable material. We develop an integrated optical amplifier-photodetector in which we exploit the photocurrent that is generated in the organic-inorganic lead halide perovskite under an applied bias. Such photocurrent does not minimally perturb the amplifier operation and is used to monitor the light signal propagating along the waveguide, for example to regulate the operation temperature.

The use of flexible materials is nowadays one of the main trends in electronics[1] and photonics,[2]and currently shows a broad range of applications,[3] such as deformable displays,[4] chip to chip interconnects,[5] mechanic tuning [6] or sensors.[7]Moreover, the implementation of a wearable photonic technology directly in contact with clothes would be light-weight,

comfortable, noninvasive, implantable and inherently low cost. It attracts a strong interest for industry in this futuristic field. Indeed, according to International Data Corporation, the important growth of this technology is forecasted to grow up to 213.6 millions in 2020.[8] Nowadays, examples of commercial real-time applications include textile-based displays,[9] photovoltaics[10] or health monitoring.[9] In spite of this significant progress wearable devices still require reduced footprint, better coupling techniques, and the integration of more complex optic/electrical functionalities to meet the performances already provided by traditional semiconductors integrated on rigid substrates.

Taking into account these current limitations, Metal Halide Perovskites (MHPs) is a promising semiconductor for flexible/wearable optoelectronic devices because of their outstanding capabilities to provide light emission, gain generation, and photodetection functionalities. Indeed, MHPs demonstrated a broad range of excellent electrical and optical properties, such as long diffusion lengths,[11] high absorption cross-section,[12] high quantum yield of emission at room temperature,[13] ort unable band-gap with the composition.[14] MHP-based devices include highly efficient solar cells, [15] optical active devices[13-14, 16] and photodetectors.[17-18] The majority of these publications, however, use a rigid substrate to fabricate the device, being it few works on MHP flexible devices with a single functionality as solar cells, [19-20] optical switch,[21]or lasing.[22] On the other hand, nanocellulose (NC)[23-24] has been probed as an ideal substrate for wearable optoelectronics.[25] This polymer is obtained from the most common biopolymer on Earth, and it consists of rigid nanocrystals that can be easily assembled into films and gel materials.NC is not only an excellent bendable, deformable and stretchable material, [26] but also exhibits very interesting properties for optoelectronics. Its advantages comprise a very high transparency in the visible,[27]tunable chiral nematic order by the surface chemistry,[28]low roughness and extremely high gas barrier properties. [29]Nevertheless, despite these promising abilities, integration of optoelectronic devices in cellulose has been elusive, being it polyimide or polydimethylsiloxane the most common flexible substrates. [30]To the best of our knowledge, there is just a single example of its use in combination with MHP for the preparation of solar cells;[31-32] with very limited performance but exhibiting a good potential for encapsulation.

In the present work, we propose a step forward in the design of wearable optoelectronic devices by the development of an integrated optical amplifier-photodetector on a biocompatible/biodegradable nanocellulose (NC) substrate, based on polymer/MHP waveguides (WGs). Our approach to integrate MHP based optoelectronics/photonics on flexible NC demonstrates: (i) an easy fabrication method to integrate the perovskite and electrodes onto a flexible and biocompatible NC substrates, (ii) a suitable design of the WG structure to enhance the optical gain of the MHP and the generated photocurrent, (iii) the successful integration of the photonic (WG-amplifier) and the optoelectronic (photodetector) components within the same flexible device, and (iv) an in situ monitoring of the photoluminescence signal inside the optical WG-amplifier through the generated carrier photocurrent.

DESCRIPTION OF THE DEVICE

The integrated WG amplifier-photodetector proposed in this work allows simultaneously the amplification of emitted light by the MHP and the signal monitoring by the photocurrent detected at metal contacts separated by the WG, as illustrated in Fig. 1a. Essentially, we exploited the optical confinement at the WG, due to the refractive index contrast between the MHP core (2.24 at 780 nm)[13], the NC bottom cladding (1.54 at 780 nm)[26] and the PMMA top cladding (1.492 at 780 nm). The WG is optimized to propagate both the excitation beam at 532 nm end fire coupled at the input edge of the sample (represented by a green Gaussian profile) as well as the generated photoluminescence (PL) at 780 nm (red PL spectrumat the bottom right corner of Fig.1a) that will propagate along the WG structure. In these conditions, light decoupled at the WG output is characterized by amplification of stimulated emission (brown spectrum at the top right corner of Fig. 1a), and the application of a bias voltage between the electrodes promotes the establishment of a photocurrent (blue data symbols at the top left corner of Fig. 1a) proportional to the excitation fluency along the WG. This compact device is implemented in a flexible NC substrate allowing bending and wearable properties (see Fig. 1b). Details about fabrication are reported in methods section and in Supplementary Information (Sec. SI1). NC was obtained by a modified version of the protocol presented in Ref. 33. Then, a compact layer (see Fig. S1) of $CH_3NH_3PbI_3$ ($MAPbI_3$) perovskite (see XRD Fig. S2) was deposited on top of NC, and then

capped by a PMMA film after patterning Au electrodes on the surface of the semiconductor. All films showed low roughness (see AFM characterization of top $MAPbI_3$ layer in Fig. 1c and a detail in Fig. S3) and good homogeneity (see SEM image in Figure 1d).

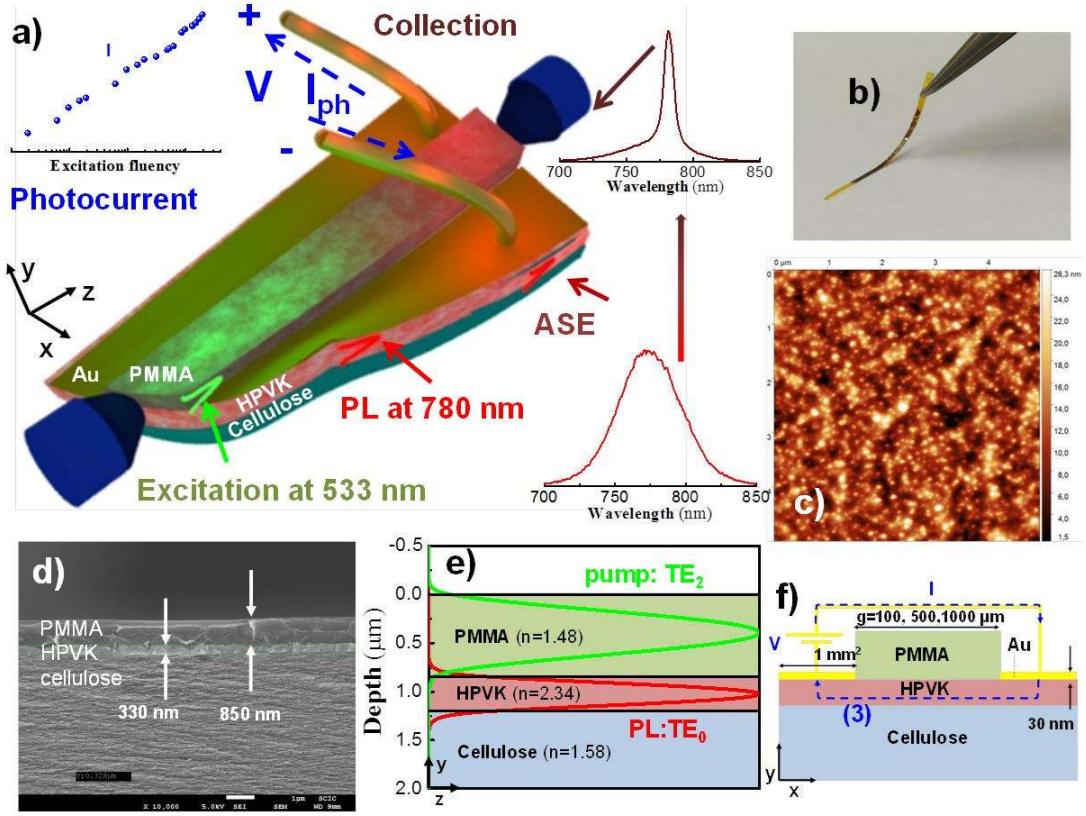

Figure 1. Description of integrated optical amplifier-photodetector.a) Scheme of the optical waveguide amplifier and photodetector integrated on NC. b) Photograph of the device on NC held on a polymer strip (without electrical contacts). c) AFM image of the MHP surface on NC. d) SEM cross section of the device. e) Longitudinal cross section of the WG and mode analysis. The low optical losses in the polymer allow the propagation of the excitation beam at 532 nm (TE_2) along the whole length of the WG (green curve), whereas the PL of the MHP at 780 nm (see red curve in a)) is excited along the WG by the evanescent field of the mode at 532 nm, and it is coupled to the TE_0 mode confined in the semiconductor (red curve); under high enough excitation fluency the WG demonstrates ASE (see brown curve in a)). f) Transversal cross section of the device with detail of the photodetector, which measures a photocurrent proportional to the applied bias voltage upon laser excitation beam propagation (blue symbols in a)).

Mode analysis carried out on a PMMA/MHP bilayer structure of 0.85/0.35 μm reveals that the pump beam at 532 nm supports the first three propagation modes in each polarization (see details in Supplementary Information SI2). These modes are spatially distributed along the semiconductor (TE_0 and TE_1) and the polymer (TE_2) with negligible

difference between the transverse electric (TE) and magnetic (TM) polarizations (thus the discussion about TE referred here can be extended to TM modes, too). Propagation at 532 nm along the TE_0 and TE_1 modes, however, is inhibited by the high absorption coefficient of the MHP at this wavelength (about 13 μm^{-1});[12-13]and hence pump beam at 532 nm mainly travels along the TE_2 mode (see green line in Fig. 1e), whose losses are reduced down to 0.05 μm^{-1}. In these conditions, evanescent field of TE_2 in the MHP (0.3 % overlap) generate PL at 780 nm along the entire length (≈1mm) of the WG. On the opposite, the TE_0 and TE_1 modes supporting the propagation of PL peaked at 780 nm are highly confined (70 % overlap) in the semiconductor (red line in Fig. 1e shows TE_0) and will promote ASE for high enough laser excitation fluencies. Indeed, we already demonstrated that the PMMA layer on top of MHP (in this case deposited on a rigid substrate) produced a double beneficial effect that assured low ASE threshold: 16 i) PMMA encapsulates the perovskite making the device stable over several months,[16] and ii)The low losses of the mode at 532 nm confined in the PMMA allows a nearly uniform excitation of the MHP layer in the WG structure. For comparison purposes a less demanding rigid system PMMA/MHP integrated in silicon has been also produced and characterized. In this configuration, a pump fluency of about 100 nJ/cm^2 corresponds to $\approx 2 \cdot 10^{20}$ photons/cm^2, which gives rise to$\approx 3.5 \cdot 10^{18}$ electrons/pulse·cm^3 from valence to conduction band ($\approx E \cdot \alpha / h\nu$, where E is the pump fluency, α the absorption coefficient and $h\nu$ the energy of the incident photon). Assuming the aforementioned uniform excitation and the geometrical parameters of the excited MHP film (100 μm wide,0.5 μm thick, 1 mm length) $1.7 \cdot 10^{11}$ electron-hole pairs/pulse will be generated in the whole waveguide at the ASE threshold. Since the passivation of grain boundaries in MHP film[34-35] lead to an enhancement of the emission quantum yield up to 70 %,[36-37] most of these pairs potentially will recombine radiatively increasing the PL signal.

Simultaneously, the application of an electric field when the MHPis optically pumped will promote a portion of those photogenerated carriers toward the external electrical circuit, i.e., give rise to an electrical photocurrent (transversal cross section in Fig. 1f). The photoresponse of the photoconductive detector under illumination is analyzed simultaneously with the PL/amplification experiment for different applied bias (the electric field can be also tuned by using different gap distance between electrodes) (see Fig. 1f). As a result, the device demonstrates photocurrents of 10-100 nA (varying slightly for different

fabricated devices and electrode gap distance) under low bias voltages (5-10 V) at the ASE threshold energy inside the WG, which is observed at ≈4nJ with a line width of around 5 nm. Indeed, we demonstrate very close performance of the subsystem fabricated on NC (micrometric-thick substrate) standing over both rigid and flexible holders/supports (thick substrates). Therefore, our approach paves the road of a future technology for wearable devices that could be directly printed on paper or incorporated in clothes or other curved surfaces by using NC as intermediate substrate.

Optical and electrical properties of MHPs on nanocellulose

MHP films deposited on NC were firstly examined under surface illumination in order to establish their optical and electro-optical properties as compared to the same films deposited on rigid substrates. The absorption coefficient of the films as a function of wavelength (left axis of Fig. 2a) presents a sharp band edge beginning at around 770 nm (1.61 eV), a visible exciton resonance at 750 nm (1.65 eV) and a monotonous increase below the band-gap wavelength, in agreement with previous publications.[12-13] Indeed, the NC substrate did not introduce any significant spectral changes as compared to the film deposited on glass, see Fig. 2a. Similarly, photoluminescence (PL) under low fluencies shows similar spectrum for both films deposited either on glass or on NC (solid lines in Fig. 2b). In both cases the MHP film exhibits ASE for high enough excitation fluencies (1 ns pulsed laser at 532 nm with 1 KHz of repetition rate), see Fig. 2b:[13,16] The Gaussian-shaped PL band centered at around 780 nm with a Full Width at Half Maximum (FWHM) around 55 nm becomes an intense and narrow Lorentzian ASE line with FWHM < 10 nm (Fig. 2b).

It is important to highlight that ASE threshold, ≈ 10 μJ/cm^2 shown in Fig. 2b, is very similar in MHP films deposited on both glass and NC substrates, as observed in the inset of Fig. 2b; this value is in agreement with a number of studies published in the last years on the $MAPbI_3$semiconductor.[38-39] This result confirms the good optical quality deduced from absorption/PL measurements on both cases. The observed slight increase of the ASE threshold of MHP deposited onto NC can be initially attributed to a higher contribution of non-radiative channels, which can be related to the smaller grain size of MHP on NC measured by AFM. According to the kinetics study shown in Fig. 2c, the experimental decay time of the PL measured on these MHP films under low excitation fluencies (below ASE

threshold) is slower when deposited in glass than in NC substrates. Indeed, the data were fitted by an effective decay time, τ_{eff}, of 13 and 6 ns for glass and NC, respectively. The exciton radiative lifetime in our MHP films results to be $\tau_r = 18.6$ *ns,* as estimated from the relation $1/\tau_{eff} = 1/\tau_r + 1/\tau_{nr}$, where τ_{nr} is the non-radiative recombination time, and the measured quantum yield ($QY = \tau_{nr}/(\tau_{nr} + \tau_r)$) of around 70 % for MHP deposited on glass, as reported elsewhere [36-37]. By taking into account that τ_r should be the same in both substrates, the non-radiative recombination time for MHP deposited on NCis $\tau_{nr}(NC) = 8.9$ *ns* (whereas $\tau_{nr}(glass) = 43$ *ns)*, which means a drop of the QY up to 32 %.

In addition, the lower thermal conductivity of NC (0.22-0.53 $Wm^{-1}\cdot K^{-1}$) [40] as compared to glass (≈1 $Wm^{-1}K^{-1}$) can also influence the ASE threshold difference. Indeed, the ASE spectra registered in the case of MHP on NC (Fig. 2b) where unstable after some minutes, as compared to the films deposited on glass that demonstrated good stability under the same laser excitation conditions. On the opposite, a stable ASE operation in MHP was observed when the repetition rate was reduced down to 100 Hz, probably because a duty cycle of 10 ms between ns-pulses allows a sufficient cooling recovery (see Supplementary Information S3).

Table I. Electrical and electro-optical properties of MHP films (350 and 500 nm thick) prepared under ambient conditions on NC and SiO_2/Si substrates. Responsivity measured through electrodes separated 0.1 and 1 mm are compared at bias voltages 2 and 20 V given its linear dependence with electric field.

		MHP on nanocellulose		**MHP on SiO_2/Si**	
		350 nm	*500 nm*	*350 nm*	*500 nm*
resistivity x 10^4 Ω·cm		1.2-12	0.3-1.9	2-35	5-20
Responsivity mA/W	g = 0.1 mm (2 V)	0.067	0.072	1.730	0.110
	g = 1 mm (20 V)	0.020	0.085	0.640	0.390

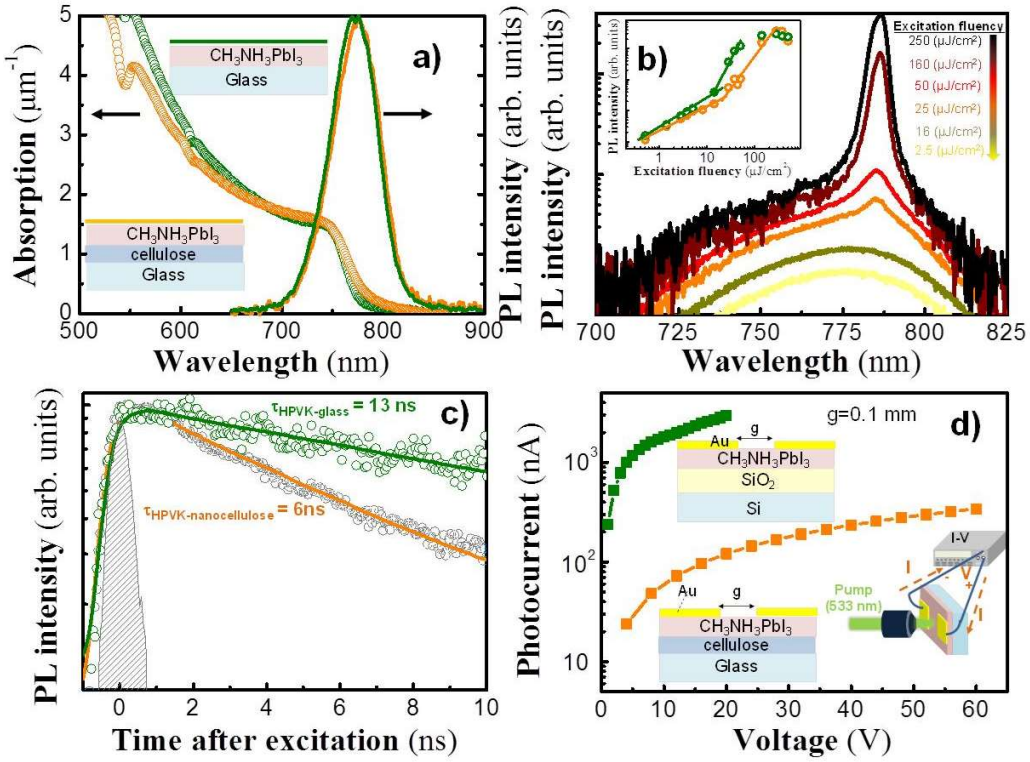

Figure 2. **Light absorption, photoluminescence and photocurrent characterization of samples and integrated devices**. a) Absorption (symbols and left axis) and PL intensity (solid lines and right axis) of a 350 nm thick MHP layers spin coated on glass (green) and NC (orange) (held on glass). b) PL spectra of MHP deposited on NC measured under back-scattering geometry (laser focused on the surface of the samples) for different excitation fluencies; above a threshold of ≈ 15 μJ/cm^2 the PL spectra narrows and its intensity grows superlinearly, clear signatures of stimulated emission; the inset compares the PL intensity as a function of the excitation fluency for MHP deposited on NC (orange symbols) and MHP deposited on glass (green symbols). c) Time resolved photoluminescence spectra of the MHP layer deposited on glass (green) and NC (orange) measured under a low excitation fluency of 30 nJ/cm^2; symbols and solid lines refer to experimental data in both samples and their corresponding exponential decay fitting; gray shaded area corresponds to the system response. d) Photocurrent as a function of the applied voltage (inset corresponds to the experimental set-up) under a CW excitation at 532 nm in a 350 nm thick MHP layer spincoated on a SiO_2/Si substrate (green symbols) and on NC (orange symbols) in a photoconductor device with a gap distance between electrodes *g= 0.1 mm*.

Several sample series were processed under ambient conditions to measure waveguided PL signal and photocurrent to check for reproducibility. Both dark current and photocurrent were measured through the deposited two metal contacts defining the photoconductor, and they yield different values of resistivity and responsivity from sample to sample, as indicated in Table 1. From I-V curves under dark conditions (see SI4 section),

the resistivity measured in most of the films are within the range $3x10^3$-$3.5x10^5$ Ω·cm, being found the larger dispersion in the case of the thinnest samples, may be due to the greater thickness inhomogeneity and surface roughness (in the case of NC). The smallest values, around $3\text{-}5x10^3$ Ω·cm, are measured in 500 nm thick films deposited on NC, which are not very different from some resistivity values reported in literature [41,42] In other samples, where the MHP was deposited either on NC or SiO_2/silicon, the resistivities were as high as 10^5 Ω·cm. In these cases, assuming a mobility of ≈10 cm^2/Vs as proposed elsewhere,[43] the electron concentration would be as low as 10^{13} cm^{-3}, which can be related to a near intrinsic semiconductor behavior.[44] In samples exhibiting this more intrinsic behavior the dark current will be smaller, hence being more sensitive to low light levels for which higher responsivity would be possible to measure. [45] In this way, a certain minimum concentration of photogenerated carriers are needed to overcome the background electron concentration in thermal equilibrium in order to give an appreciable photocurrent density J_{ph} ($J_{illumination}= J_{dark}+J_{ph}= e\mu_n n_0 + e\mu_n \Delta n$), assuming a n-type character for the MHP,[17-18] consistently with better responsivity values measured in more resistive films (Table I).

In MHP films under low illumination level (60 mW/cm^2 at 532 nm under normal incidence, see inset in Fig. 2d) exhibit a noticeable photocurrent of ≈2.10^3 and ≈10^2 nA (at 15 V of bias voltage, i.e., low applied electric field ≈ 1.5kV/cm) in SiO_2/Si and NC substrates, respectively, as observed Fig.2d. The lower photocurrent of the films deposited on NC is again attributed to nonradiative carrier losses, but also to the smaller resistivity (higher dark current in this NC sample) and the worse thermal conductivity of NC.

The temporal response of the device seems to be limited by the RC constant of the photoconductive detector circuit (R = 1 MΩ – C = 330pF), because it is observed a frequency bandwidth below 1 KHz, and the RC constant of the photoconductive device itself that gives a time constant of around 20 μs due to the high resistivity of the MHP film, as illustrated in Fig. SI8, at least for the excitation laser used in the experiments with 20 kHz of repetition rate. In any case, this is not a limitation factor for the concept device demonstrated in this work and future improvements are possible by optimizing both factors (photodevice and its external circuit).

Integrated amplifier/photodetector device on nanocellulose: applications

The MHP amplifying device fabricated on NC was studied under end-fire coupling of a pulsed laser pumping at 532 nm (WG geometry, as shown in Fig. 3a). In these conditions the ASE signal collected from the output edge of the WG as a guided mode (see Fig. 3b) exhibits a narrow peak (whose linewidth is 5 nm for the highest laser excitation power used in the experiment, as indicated in Fig. 3c) that grows superlinearly above a threshold of ≈ 4 nJ, as observed in Fig. 3d. This behavior is quite similar as the one observed above under backscattering geometry and previously reported in similar structures integrated on a Si/SiO_2 rigid substrate.[16] Such a superlinear growth of the PL intensity (blue solid circles in Fig. 3d) would follow a potential increase $I_{PL} \propto I_{PUMP}^{2.5}$, which would correspond to a gain G =10 dB/cm at the output edge of the waveguide (L≈1 mm long) [16] or, in other words, a modal gain (g) of 23 cm^{-1} ($G(dB)=10log(e^{g \cdot L})$), close to the material gain ($g=\Gamma \cdot g_m$) since the confinement factor of the optical modes in the MHP film is close to 1. Here it is worth mentioning that PL intensity was stable during the measurement, although similar excitation conditions (20 kHz excitation source) did not show a stable ASE production under backscattering geometry. Therefore, the high confinement of emitted light by the active medium provided by this WG structure enhances the generation of light, and triggers the ASE regime. Moreover, the excitation fluencies shown in Figs. 3c-dcorrespond to excitation light coupled with the whole PMMA/MHP/NC structure with a cross section of about $2 \cdot 10^{-5}$ cm^2. Nevertheless, since this device propagates the light along the PMMA layer, only a 0.3 % of the TE_2 mode at 532 nm travels along the MHP, reducing the thermal heating of the semiconductor and the effective ASE threshold (E_{th}) down to 600 nJ/cm^2 (one order of magnitude smaller than that measured under backscattering geometry in Fig. 2b). This E_{th} corresponds to an average power of the external pumping laser as low as 0.8 mW, which is estimated by taking into account a coupling efficiency ≈ 10 % inside the waveguide and the repetition rate (20 KHz) of the pulsed laser.

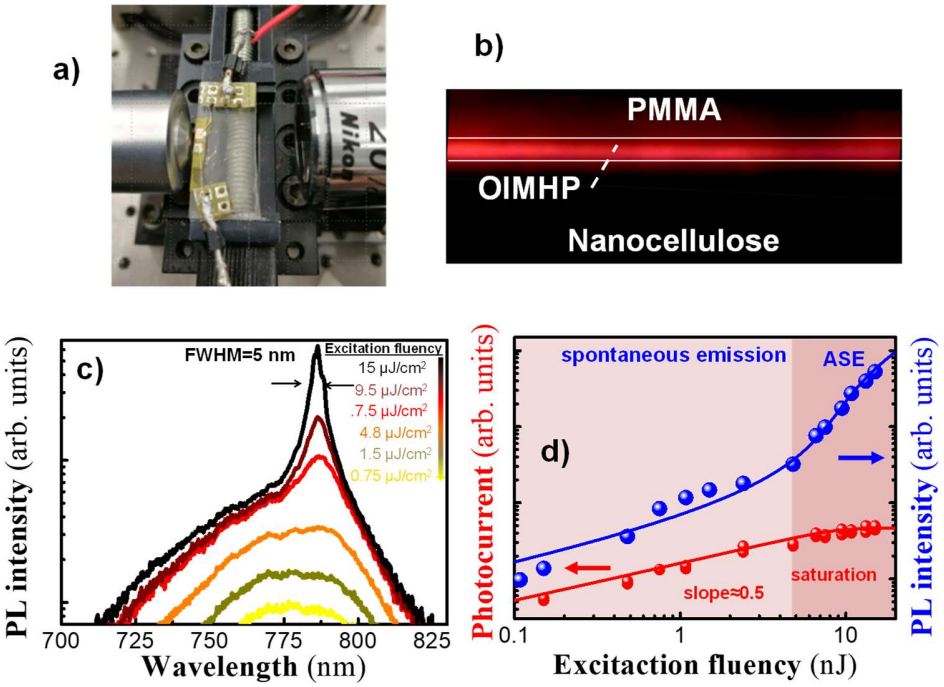

Figure 3. **Characterization and modelling of the flexible device**. a) Picture of holder and photo-device with end-fire excitation/collection objectives. b) PL decoupled at the output edge of the waveguide.c) PL intensity measured for different excitation fluencies collapses to a narrow peak of about 10 nm above a certain threshold. d) PL intensity (blue symbols) as a function of the excitation fluency demonstrates a superlinear growth of the PL above the 4 nJ threshold, while photocurrent shows a sublinear increase (red symbols) before saturation, in agreement with the model (solid lines), as explained in the text; photocurrent was measured by applying 10 V on gold electrodes with *g=1 mm*.

Under the above given excitation conditions, the photocurrent mainly monitors photogenerated carriers by the pump beam travelling along the 1 mm long PMMA/MHP WG, the same distance covered by the Au-electrodes. The photocurrent variation presented in Fig.3d indicate a clear correlation between I_{PL} and I_{PC}: the experimental I_{PC} (red data symbols in Fig. 3d) clearly follows a square root law ($I_{PC} \propto I_{PUMP}^{1/2}$) before the saturation observed above E_{th}. Moreover, I_{PC} and I_{PL} dependences can be nicely fitted (solid lines in Fig. 3d) with the model developed in SI6. The simulations reveal a transparency carrier concentration for stimulated emission $N_0 \approx 1.5 \times 10^{18}$ in agreement with previous results.[16] This square root law for I_{PC} as a function of the excitation fluency corresponds to the high carrier injection regime, while its saturation is attributed to the gain saturation mechanism in optical amplifiers, [25] where the increment of photogenerated carriers over N_0 is transformed into photons (stimulated emission regime). In this way, the highest excitation fluencies reveal I_{PC}

up to 25-50 mA/cm^2 for 100-600 V/cm applied electric fields inside the waveguide. Finally, it is worth mentioning that the device-on-NC presents again features very close to those obtained for MHP films on rigid substrates (see Supporting Information SI7), except a slightly higher peak energy threshold (4 instead of 2 nJ) and ASE linewidth (5 nm instead 2-3 nm) and higher photocurrents.

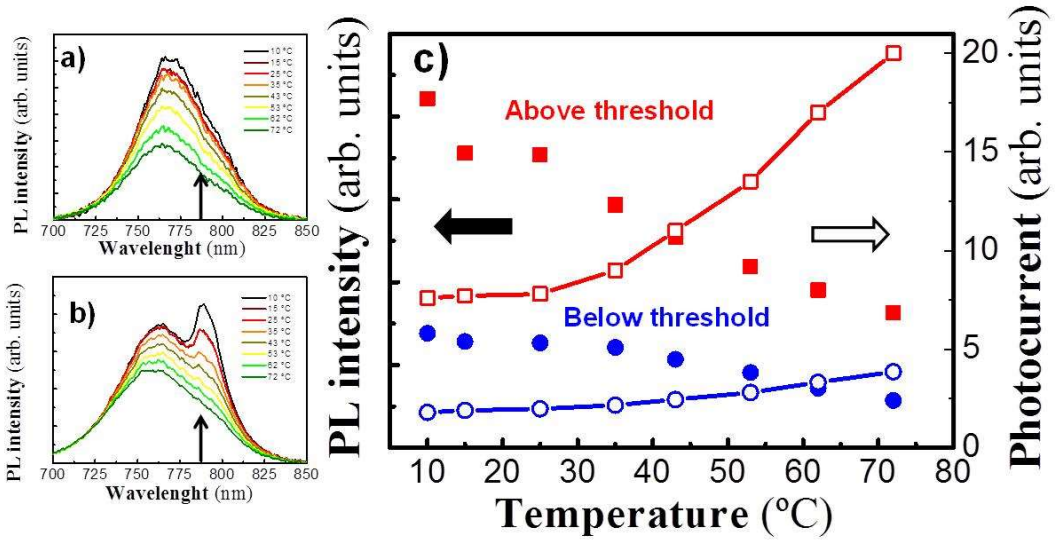

Figure 4. Control of operation temperature of the photodevice. a)-b) Evolution of PL spectra well below (a)and just above (b) the threshold of ASE for temperatures between 10 and 72 ºC. c) PL intensity measured at 790 nm (filled symbols) and photocurrent (empty symbols) as a function of temperature below (blue) and above (red) the ASE threshold; the lines are guides for the eyes. Temperature measurements were done by using a Peltier device with area 1 cm^2.

The integrated amplifier-photodetector device can be used for many applications related to signal amplification and processing at 780-790 nm (telecom, sensing and other fields) but also at shorter/longer wavelengths by changing the metal or the halide in the MHP compound. A primary use would be the control itself of the optical amplifier to fix the threshold of operation, specially under temperature changes, as demonstrated in Fig. 4. If laser fluency is fixed below the threshold the PL peak intensity decreases above room temperature (spectra in Fig. 4a and blue solid circles in Fig. 4c), whereas the photocurrent measured simultaneously at the photodetector suffers a slight monotonous increase (blue

hollow circles in Fig. 4c), as expected if the population of free carriers increases with temperature as compared to that of free excitons. However, if laser fluency is fixed just above the threshold, the PL peak at the ASE wavelength decreases in a similar way (spectra in Fig. 4b and red solid squares in Fig. 4c), but this time the photocurrent is practically constant up to room temperature (red hollow squares in Fig. 4c), due to its saturation regime (see above), and increases much faster when increasing temperature because the ASE regime is progressively lost against spontaneous emission.

Conclusions

In this work, we propose the monolithic integration of a WG amplifier-photodetector system in a flexible nanocellulose substrate for future wearable applications. The device allows an in-situ monitoring of PL signal (in spontaneous and ASE regimes) decoupled at the edge of the waveguide by studying the photocurrent generated by the pump beam generating this PL. For this purpose, we successfully integrated aPMMA/$MAPbI_3$ bilayer structure on the cellulose substrate without any significant degradation of the semiconductor, and inject the excitation light at the input edge of the flexible substrate. As a result, ASE is demonstrated with similar performances as those reported forrigid substrates. Moreover, we demonstrate the simultaneous photodetection of light photogenerating carriers in the MHP film by means of the integrated photoconductor with the WG amplifier. The resulting photocurrent demonstrates a clear correlation with the intensity of PL under spontaneous and ASE generation regimes as a function of the laser excitation fluency. Moreover, the different behaviors of the photocurrent in the two regimes will allow different applications, such as trigger generation, gain automatic control, signal processing for visible telecommunications and sensing. This control is demonstrated by varying temperature below and above room temperature. Therefore, the present work pave the road for the future integration of wearable photonic components using cellulose substrates.

METHODS

Products and substrate preparation

All chemicals were used as received. N,N-dimethylformamide (DMF) anhydrous, 99.8% , Dimethyl sulfoxide (DMSO) anhydrous ≥99.9%, Toluene anhydrous, 99.8% and Poly(methyl methacrylate) (PMMA) with average molecular weight of 350000 were purchased from Sigma-Aldrich, methylammonium iodide (MAI) was purchased from DYESOL, and PbI2 99.99%, was purchased from TCI. MHP solutions with concentrations of 1.35 and 2.025 M were prepared by adding 1 mL of DMF and 95 μL of DMSO into each vial containing 622 and 933 mg of PbI_2. The solutions were heated at 65°C to dissolve PbI_2. After cooled down to the room temperature, they were poured into corresponding vials containing 215 and 322.5 mg of MAI to make final solutions. PMMA solutions with concentrations of 99, 110 and 140 mg/ml in Toluene were prepared by stirring. Plain glass and commercial SiO_2(2 μm)/Si substrate (supplied by Activebizz, Germany) substrates were cleaned and sonicated for 15 min in a solution of Milli-Q (distilled) water and soap (Hellmanex), rinsed with Milli-Q water, sonicated for 15 min in ethanol, rinsed with acetone and dried with compressed air.

Device fabrication

Cellulose nanocrystals were obtained via TEMPO-mediated oxidation, using a procedure slightly modified from the original one proposed. The initial aqueous solution was composed by 10 g of Kraft pulp immersed in 1 L of purified water and stirred with a magnetic stirrer for half an hour. Later, the solution was sonicated for other 30 minutes in a 350 Watt ultrasonic bath, obtaining a preliminary homogeneous suspension of cellulose. Oxidant and catalyst species (0.162 g of TEMPO, 1.000 g of NaBrand 35ml of NaClO) were added to the solution under stirring. The pH was monitored during the reaction and maintained at a value between 10.5and 11 through the addition of 1 ml of 1M NaOH at time. Once stabilized, the pH was neutralized by diluting the solution and letting the cellulose to deposit on the bottom of the bicker and then washed with purified water: the washing was repeated 15times with at least 400 ml of water each. Cellulose concentration was measured weighting a known quantity of solution, subsequently placed in a oven at 60°C. Once completely dried, the remaining cellulose was weighted again. Typical values were in the range 3-5 mg/mL. The concentration can be tuned by either dilution or concentration through water evaporation. The mechanical disintegration to release the nanofibers was reached through sonication using

a Bandelin Sonopuls HD 2200 ultrasonic homogenizer with a 13 mm diameter ultrasonic tip for 2 minutes at 20kHz frequency and100W output power. This step was repeated twice for every sample, obtaining transparent NC fibrils suspension. Finally, the films were obtained by pouring the clear suspension on a 8.5 cm diameter Petri dish and drying it at 60°C in an oven. The oven was equipped with a flat copper foil to maintain homogeneous temperature over the whole layer surface. The solution dried for 36 hours, at the end a transparent and homogeneous film could be peeled off. These were stored at room temperature in a dehumidified container. To be handled NC films need to have 10-20 μm of thickness. This can be obtained by varying either the amounts of the poured solution or by changing the NC concentration. Samples used for the perovskite deposition were 20 μm thick, see SI/ section for more details.

Then, NC was attached to glass substrates by using double sided tape at margins. In order to have a uniform and homogeneous layer of perovskite on plain glass and NC, substrates were ozone treated for 15 min just before spin coating of perovskite. MHP films were deposited by spin-coating of 50 μl of 1.35 and 2.025 M solutions for 50s at 4000 and 3000 rpm respectively. During spin coating, anti-solvent method was employed in order to help in the film crystallization, washing with non-polar diethyl ether just before formation of white crystals in the substrate. At 30 and 60% R.H, this could be relatively 8-9 and 12-13 seconds after starting the spin coating. Then substrates were annealed at 100 °C for 3 minutes. At the end of the process 350-500 nm thick $MAPbI_3$ films (thickness is controlled with the spin coating speed) were deposited on the NC. Once the perovskite was properly deposited on the flexible substrate, 1 mm^2 square and 30 nm thick Au electrodes were evaporated on the semiconductor. Then, gaps of 100 μm, 500 μm and 1 μm were patterned by protecting the sample with an aluminum mask. Finally a ≈1 μm thick Poly(methyl methacrylate) (PMMA) film is spin coated for 3000 rpm on the perovskite as capping layer and post baked at 80 ºC and 150 ºC each temperature. Here electrodes were protected with a resist before PMMA deposition to enable the final bonding of Au wires with silver taint. The biocompatibility and flexibility of the cellulose substrate allows the-device-on-cellulose to be easily wore on or incorporated to any kind of substrate or surfaces. Here it was deposited on a rigid polymer strip (one side glued) to allow an easier examination of the optical electrical properties. For this purpose, edges of the sample were carefully cut with a thin blade from the back side

(polymer strip). For electrical measurements, the whole device-on-cellulose/polymer stripe structure was pasted on glass in order to allow an easier bonding of Au wires and the electrical connections.

Structural characterization

The morphology of the films was analyzed by SEM using a JSM7001F (field emission scanning electron microscope). The XRD patterns of the samples were measured using a X-ray diffractometer (D8 Advance, Bruker-AXS) (Cu Kα, wavelength λ= 1.5406 °A).

Optical characterization

The device is examined at room temperature and ambient conditions by end-fire coupling a Nd:Yag laser doubled at 532 nm (SNP-20F-100 supplied by Team Photonics, France) at the input edge of the sample (pulse of 1 ns 20 KHz repetition rate) with the aid of 40x microscope objective, see Fig. 1a. The waveguide PL of the $MAPbI_3$ at 780 nm, Fig. 1a, is collected at the output edge of the structure with a 20x microscope objective and focused into a fiber optic connected to a HR4000 Ocean Optics spectrograph (estimated overall resolution better than 0.7 nm). Time resolved PL was carried out by focusing the PL into a Hamamatsu C5658-3769 avalanche photodetector connected to a BOXCARDPCS-150 electronics from Becker &Hickl GmbH. Textural. Photocurrent, see Fig. 1a, is analyzed by applying an electric field between the Au electrodes and measuring the generated current by using a Keithley's Series 2400 Source Measure Unit (SMU). Detection below 2 nA is limited by the dark current of the device and resolution of the multimeter. Frequency dependence experiments were carried out by illuminating the samples under Continuous Wave (CW) excitation at 532 nm (Z40M18-B, Z-laser Optoelektronic GmbH, Germany) chopped at a controlled frequency. Then photocurrent generated by the application of the external voltage with the SMU is synchronously detected with a lock-in amplifier (SR810, StandFord Research Systems) by previously filtering the DC component with a RC circuit. Time dependence electrical experiments were performed by detecting the photocurrent with the scope GDS-8208 (GW Instek, Taiwan). Additional characterization was performed by focusing the excitation beam on the top of the sample and measuring the back-scattering PL/photocurrent with the same set-up. In addition, samples were also examined under CW excitation at 532 nm, and 1 ns

pulsed Nd:Yag laser doubled at 532 nm with variable repetition rate 100-1 KHz (FTSS355-Q4-1KHZ adapted at 532 nm and supplied by CryLas Laser Systems, Germany).

---

[1] Rogers J.A., Someya T. and Huang Y. Materials and mechanics for stretchable electronics. *Science***327**, 1603-1607 (2010)

[2] http://spie.org/newsroom/wearable-photonics?pf=true

[3] Hu J., Li L., Lin H., Zhang P., Zhou W. and Ma Z. Flexible integrated photonics: where materials, mechanics and optics meet. Opt. Express **3**, 1313-1331 (2013)

[4] Park S.I., Xiong Y., Kim R.H., Elvikis P., Meitl M., Kim D,H., Wu J., Yoon J., Yu C.J., Liu Z., Huang Y., Hwang K.C., Ferreira P., Li X., Choquette K. and Rogers J.A. Printed assemblies of inorganic light-emitting diodes for deformable and semitransparent displays. *Science***325**, 977-981 (2009)

[5] Bosman E., Van Steenberge G.V., Van Hoe B., Missine J., Vanfleteren J. and Van Daele P. Highly reliable flexible active photonic links. IEEE Phot. Tech. Lett. 22, 287-289 (2010)

[6] Chen Y., Li H. and Li M. Flexible and tunable silicon photonic circuits on plastic substrates. Scientific Reports 2, 622 (2012)

[7] Shih M.H., Hsu K.S., Kunag W., Yang Y.C., Tsai S.K., Liu Y.C., Chang Z.C. and Wu M.C. Compact optical curvature sensor with a flexible microdisk laser on a polymer substrate. Opt. Lett. 34, 2733-2735 (2009).

[8] http://www.idc.com/getdoc.jsp?containerId=prUS41530816

[9] http://www.laserfocusworld.com/articles/print/volume-48/issue-04/features/smart-photonic-textiles-begin-to-weave-their-magic.html

[10] http://sauletech.com/

[11] Dong Q., Fang Y., Shao Y., Mulligan P., Qiu J., Cao L. and Huang J. Electron-hole diffusion lengths >175 μm in solution-grown $CH_3NH_3PbI_3$ single crystals. *Science***347**, 967-970 (2015).

[12] De Wolf S., Holovsky J., Moon S.J., Löper P., Niesen B., Ledinsky M., Haug F.J., Yum J.H. and Ballif C. Organometallic halide perovskites: sharp optical absorption edge and its relation to photovoltaic performance. *J. Phys. Chem. Lett.***5**, 1035-1039 (2014).

[13] Xing G., Mathews N., Lim S.S., Yantara N., Liu X., Sabba D., Grätzel M., Mhaisalkar S. and Sum T.C. Low-temperature solution-processed wavelength-tunable perovskites for lasing. Nat. Photon. **13**, 476–480 (2014).

[14] Zhu H., Fu F., Meng F., Wu X., Gong Z., Ding Q., Gustafsson M.V., Trinh M.T., Jin S. and Zhu X.Y. Lead halide perovskite nanowire lasers with low lasing thresholds and high quality factors. *Nat. Mater.***14**, 636–642 (2015).

[15] NREL, 2016, http://www.nrel.gov/ncpv/images/efficiency_chart. jpg, accessed: April 2016 .

[16] Suárez I., Juárez-Pérez J., Bisquers J., Mora-Seró I. and Martínez-Pastor J.P. Polymer/perovskite amplifying waveguides for active hybrid silicon photonics. *Adv. Mater.***27**, 6157-6162 (2015).

[17] Lin Q., Armin A., Burn P.L. and Meredith P.Filterless narrowband visible photodetectors. *Nat. Photon.***9**, 687-695 (2015)

[18] Fang. Y., Dong Q., Shao Y., Yuan Y. and Huang J. Highly narrowband pervovskite single-crystal photodetectors enabled by surface-charge recombination. *Nat. Photon.***9**, 679-687 (2015).

[19] Di Giacomo F., Fakharuddin A., Jose R. and Brown T.M. Progress, challenges and perspectives in flexible perovskite solar cells. *Energy Environ. Sci.***9**, 3007--3035 (2016).

[20]Kaltenbbrunner M., Adam G., Glowacki E.D., Drack M.,Schwödiauer R., Leonat L., Apaydin D.H., Groiss H., Scharber M.C., White M.S., Sariciftci N.S. and Bauer S. Flexible high power-per-weight perovskite solar cells with chromium oxide-metal contacts for improved stability in air.*Nat. Mater.***14**, 1032–1039 (2015)

[21] Cong L., Srivastava Y.K., Solanki A., Sum T.C. and Singh R. Perovskite as a platform for active metaphotonic devices. ACS Photonics, 4, 1591-1601 (2017).

[22]Stranks S.D., Wood S.M., Wojciechowski K., Deschler F., Saliba M., Khandelwal H., Patel B.J., Elston S.J., Herz L.M., Johnston M.B., Schenning A.P.H.J., Debije M.G., Riede M.K., Morris S.M. and Snaith H.J. Enhanced amplified spontaneous emission in perovskites using a flexible cholesteric liquid crystal reflector. *Nano Lett.***15**, 4935-1941 (2015).

[23]Klemm D., Kramer F., Moritz S., Lindström T., Ankerfors M., Gray D. and Dorris A.Nanocelluloses: A New Family of Nature-Based Materials. *Angew. Chem. Int. Ed.* 50, 5438 – 5466 (2011)
[24]Dufresnce A. Nanocellulose: a new ageless bionanomaterial. Materials Today 16, 220-227 (2013)
[25] Abitbol T., Rivkin A., Cao Y., Nevo Y., Abraham E., Ben-Shalom T., Lapidot S. and Shoseyov O. Nanocellulose, a tiny fiber with huge applications. *Curr. Opin. Bbiotechnol.* **39**, 76-88 (2016).
[26]Bettotti P., Maestri C.A., Guider R., Mancini I., Nativ-Roth E., Golan Y. and Scarpa M. Dynamics of hydration of nanocellulose films. *Adv. Mater. Interfaces***3**, 1500415 (2015).
[27]Wu W., Tassi N.G., Zhu H., Fang Z. and Hu L. Nanocellulose-based translucent diffuser for optoelectronic device applications with dramatic improvement of light coupling. *ACS Appl. Mater. Interfaces***7**, 26860-26864 (2015).
[28]Guidetti G., Atifi S., Vignolini S. and Hamad W.Y. Flexible photonic cellulose nanocrystal films. *Adv. Mater.***28**, 10042-10047 (2016).
[29]Roilo D., Maestri C.A., Scarpa M., Bettotti P., Werner E., Tönjes K., Brusa R. and Checchetto P. Cellulose Nanofibrils Films: Molecular Diffusion through Elongated Sub- Nano Cavities. *J. Phys. Chem. C***121**, 15437–15447 (2017).
[30] YangY., YangX. and Yuan Q. Recent progress in flexible and wearable bioelectronics based on nanomaliterial.*Nano Res.***10**, 1560-1583 (2017)
[31]Jung M.H., Park N.M. and Lee S.Y. Color tunable nanopaper solar cells using hybrid $CH_3NH_3PbI_{3-x}Br_x$perovskite. *Solar Energy***139**, 458–466(2016).
[32] Castro-Hermosa S., Dagar J., MarsellaA.and Brown M.T. Perovskite Solar Cells on Paper and the Role of Substrates and Electrodes on Performance. *IEEE Electron Device Lett.***38**, 1278-1281 (2017).
[33]Saito T., Kimura S., Nishiyama Y. and Isogai Y. Cellulose nanofibers prepared byTEMPO-mediated oxidation of native cellulose. Biomacromolecules**8** 2485–2491(2007)
[34] Ngo T.T., Suárez I., Antonicelli G., Cortizo-Lacalle D., Martinez-Pastor J.P, Mateo-Alonso A. and Mora-Sero I. Enhancement of the Performance of Perovskite Solar Cells, LEDs, and Optical Amplifiers by Anti-Solvent Additive Deposition. *Adv. Matter.* **29**, 1604056 (2017).
[35]Pourdavoud N., Wang S., Mayer A., Hu T., Chen Y., Marianovich A., Kowalsky W., Heiderhoff R., Scheer H.C., and Riedl T. Photonic Nanostructures Patterned by Thermal Nanoimprint Directly into Organo-Metal Halide Perovskites. *Adv. Matter.* **29**, 1605003 (2017).
[36]Deschler F., Price M., Pathak S., Klintberg L.E., Jaraush D.D., Higler R., Hüttner S., Leijtens T., Stranks S.D., Snaith H.J., Atatüre M., Philips R.T. and Friend R.H. High photoluminescence efficiency and optically pumped lasing in solution-processed mixed halide perovskite semiconductors. *J. Phys. Chem. Lett.***5**, 1421-1426 (2014).
[37]Daguta S., Thankur S., Morozov Y.V., Wang Y., Manser J.S., Kamat P.V. and Kuno M. Spatially non-uniform trap state densities in solution-processed hybrid perovskite thin films. J. Phys. Chem. Lett. 7, 715-721 (2016).
[38]Sutherland B.R. and Sargent E.H. Perovskite photonic sources. *Nat. Photon.***10**, 295-302 (2016)
[39]Suárez I. Active photonic devices based on colloidal semiconductor nanocrystals and organometallic halide perovskites. *Eur. Phys. J. Appl. Phys.***75**, 30001 (2016)
[40]Diaz J.A., Ye Z., Wu X., Moore A.L., Moon R.J., Martini A, Boday J.L. and Youngblood J.P. Thermal conductivity in nanostructured films: from single cellulose nanocrystals to bulk films. *Biomacromolecules***15**, 4096−4101 (2014)
[41]Juárez-Pérez E.J., Sánchez R.S., Badia L., García-Belmonte G., Kang Y.S., Mora-Seró I. and Bisquert J. Photoinduced Giant Dielectric Constant in Lead Halide Perovskite Solar Cells. *J. Phys. Chem. Lett.***5**, 2390–2394 (2014).
[42]A. Jaffe,Y. Lin,C. M. Beavers,J. Voss,W. L. Mao, and H. I. Karunadasa, High-Pressure Single-Crystal Structures of 3D Lead-Halide Hybrid Perovskites and Pressure Effects on their Electronic and Optical Properties, ACS Cent. Sci. **2**, 201−209 (2016).
[43]Motta C., El-Mellouhi F. and Sanvito S. Charge carrier mobility in hybrid halide perovskites. *Scientific Reports***5**, 12746 (2015).
[44]M. V. Khenkin, D. V. Amasev, S. A. Kozyukhin, A. V. Sadovnikov, E. A. Katz, and A. G. Kazanskii, Temperature and spectral dependence of $CH_3NH_3PbI_3$ films photoconductivity, *Appl. Phys. Lett.* 110, 222107 (2017).
[45]S. A. MCDonald, G.Konstantatos, S. Zhang, P.W. CYR, E.J.D. Klem, L.Levinaand E.H. Sargent, Solution-processed PbS quantum dot infrared photodetectors and photovoltaics. Nat. Matter. 4, 138-142 (2005).